Three-dimensional nanocomposites of graphene/carbon nanotube matrix-embedded Si nanoparticles for superior lithium ion batteries

Dafang He[1,2], Lixian Li[1], Fengjuan Bai[2], Chenyang Zha[1], Liming Shen[1],
Harold H. Kung[3], Ningzhong Bao[1*]

[1]*State Key Laboratory of Material-Oriented Chemical Engineering, College of Chemistry and Chemical Engineering, Nanjing Tech University, Nanjing, Jiangsu 210009, P. R. China.*
[2]*Jiangnan Graphene Research Institute, Changzhou, Jiangsu 213149, P. R. China*
[3]*Department of Chemical and Biological Engineering, Northwestern University, Evanston, Illinois 60208, USA*

[*]Corresponding author. Tel/fax: +86-25-83172244. E-mail: nzhbao@njtech.edu.cn

Received: 21 August 2016, Revised: 20 October 2016 and Accepted: 22 November 2016

DOI: 10.5185/amlett.2017.7038
www.vbripress.com/aml

Abstract

A unique hierarchically nanostructured composite of Si nanoparticles (Si NPs) embedded in a three-dimensional (3D) carbon nanotube (CNT)/graphene sheet (GS) matrix (Si@CNT/GS) is fabricated by freeze-drying and thermal reduction. In this novel nanostructured composite, since the intertwined elastic CNTs effectively disperse the Si NP anode material and provide extra physical connections between Si NPs and the surrounding 3D conductive matrix, the interconnected 3D CNT/GS matrix can serve to buffer the volume change of the Si NPs during cycling while simultaneously enhance the electrical conductivity of the overall electrode. As a result, Si@CNT/GS nanocomposite exhibits a high reversible capacity of 1362 mAh·g^{-1} at 500 mA·g^{-1} over 500 cycles, and an excellent rate capability of 504 mAh·g^{-1} at 8400 mA·g^{-1}, considerably improving the battery performance compared with those electrodes made from Si@graphene nanocomposites, thus exhibiting great potential as an anode composite structure for lithium storage. Copyright © 2017 VBRI Press.

Keywords: Nanocomposites, silicon nanoparticles, graphene, carbon nanotube, lithium ion battery.

Introduction

Despite great progress in the performance of lithium-ion batteries (LIBs), their capacity and cycle life remain as critical challenges for applications in various electrified vehicles [**1-3**]. The conventional carbonaceous anode material with low capacity (372 mAh·g^{-1}) and poor rate capability stands far from meeting the increasingly stringent demand of the next-generation LIBs [**4**]. Various anode materials with higher specific capacities have been reported for lithium-ion batteries. Among them, silicon is considered one of the most promising owing to its natural abundance, outstanding safety, and exceptionally high theoretical specific capacity of 3579 mAh·g^{-1} for $Li_{15}Si_4$ at room temperature [**5-7**]. However, the implementation of silicon anode has been hindered by large volume expansion (>300%) during lithiation/delithiation and its low intrinsic electronic conductivity that result in dramatic pulverization of Si particles and electrical disconnection from the current collector, leading to rapid capacity fade upon cycling [**8,9**]. To overcome these obstacles, Si nanostructures were fabricated including nanowires [**10,11**], nanotubes [**13-14**], and nanoporous structures [**15,16**], and preparation of high-conductivity carbon-coated Si nanocomposites [**17,18**] have been extensively studied. However, even though these porous structures improve strain tolerance and electron transport while suppressing the mechanical fracture, their cycling stability remains unsatisfactory.

Two dimensional graphene and one dimensional carbon nanotube (CNT) are both intriguing carbonaceous materials with unique nanostructures. Graphene has been confirmed to be an ideal multifunctional support material used with Si nanoparticles as anode for LIBs, owing to its large specific surface area, excellent electrical conductivity, superior mechanical flexibility, and high chemical and thermal stability [**19-22**]. Carbon nanotubes can be thought of as multiple rolled layers of graphene nanosheets, and there are numerous studies of CNT-based silicon anode materials [**23-24**]. In particular, Kung and his co-workers prepared a three-dimensional (3D) Si nanoparticle-graphene paper composite by a filtration-directed assembly approach to produce a material with greatly improved lithium storage capacity, exhibiting a high reversible capacity of 1100 mAh·g^{-1} at 8 A·g^{-1} over 150 cycles [**25-26**]. Very recently, we developed a simple method to fabricate magnesiothermo-reduced silicon nanoparticles/graphene sandwich-structure which partially alleviated the pulverization induced by the volume change of silicon, although the capacity decay remained problematic when the LIBs were operated at a high rate and over a large number of cycles [**27**]. These magnesiothermo-reduced Si NPs suffer from the disadvantages of large particle sizes and a certain degree of agglomeration, causing both an increase in the absolute volume change and a decreased electrolyte/Si interfacial area as compared with more dispersed Si NPs, and eventually leading to structural collapse during the Li ion insertion/extraction process.

In this work, we chose commercial Si NPs of much smaller particle size and high dispersity compared with the magnesiothermo-reduced Si NPs, and fabricated a novel nanostructured composite of Si NPs embedded in a 3D CNT/graphene sheet (GS) matrix (Si@CNT/GS). Frist, nanosized structures not only can shorten the diffusion pathways of the lithium ions, facilitating rapid lithiation and delithiation processes, but also can significantly reduce the mechanical stress of the materials during cycling. The pulverization of silicon is prevented when their size is very small. Second, we did not modify the carbon nanotubes, thus avoiding the defects caused by the modification of the carbon nanotubes which caused the reduced conductivity. Finally, **Fig. 1** shows a schematic drawing of the hierarchical 3D structure of the Si@CNTs/GS nanocomposite, in which Si NPs are confined within the 3D CNT/GS nanostructure matrix. The intertwined elastic CNTs effectively disperse the Si NPs inside the matrix and provide additional physical and electrical contact between Si NPs and the 3D conductive matrix framework. The 3D CNT/GS matrix framework buffers the volume change of the Si NPs during cycling while enhance the electrical conductivity of the overall electrode. As a result, Si@CNT/GS can deliver a high reversible capacity of 1362 mAh·g^{-1} at 500 mA·g^{-1} over 500 cycles, with excellent rate capability of 504 mAh·g^{-1} at 8400 mA·g^{-1}, thus exhibiting great potential as an anode composite structure for lithium storage refer to **Table S1**.

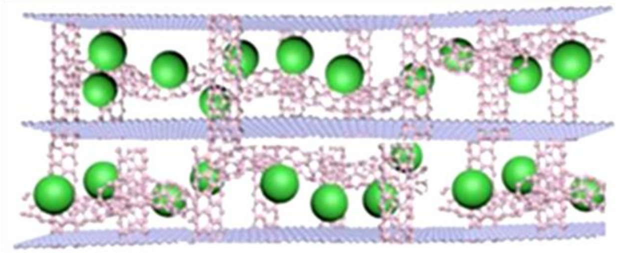

Fig. 1. Schematic drawing (not to scale) of a section of the Si@CNT/GS nanocomposites consisting of Si nanoparticles (large green spheres) embedded in a 3D CNT/GS nanostructured framework.

Experimental

Materials

All chemicals, including nano-silicon (Xuzhou Jiechuang New Material Tech Co., Ltd), CNT powder (Aladdin Ltd.), 1 mg/mL graphene oxide aqueous dispersion (A&W MaTech Co., Ltd.) were used as-received without further purification.

Material synthesis

60 mg nano-Si was dispersed in 60 mL water by sonication for 10 min (2000w, 40kHz), and 15 mg CNT powder was dispersed in 15 mL water separately by sonication for 120 min. These two dispersions were then added into 30 mL of graphene oxide aqueous dispersion (1 mg/mL) and the mixture was gently sonicated for another 120 min, followed by the freeze-drying. The freeze dried sample was placed in a crucible inside a tube furnace, heated to 900 °C at a heating rate 10 °C·min^{-1} under Ar atmosphere, and kept at the temperature for 2 h for thermal reduction. The as-synthesized 3D Si@CNT/GS nanocomposites were stored in a glovebox.

Characterizations

Raman spectra were collected with a J-YT640000, John Yvon Raman laser spectrometer using 514.5 nm laser excitation. The crystalline phase and structure of powder samples were characterized by X-ray diffraction (XRD) using a D8-Advance, Bruker AXS diffractometer (Cu-Kα radiation, λ=1.5418 Å, 40 kV, 100 mA, from 2θ=5° to 80°, scan-speed 0.8 sec/step, and increment of 0.02 deg/s). The morphology and microstructure were characterized by optical microscopy, field emission scanning electron microscopy (FESEM, HITACHI S−4800), and transmission electron microscopy (TEM, JEOL JEM−2100). Thermogravimetric analyses (TGA) were performed on a NETZSCH STA 449C thermogravimetric analyzer. The samples (12 mg) were heated in air from room temperature to 800 °C at 10 °C·min^{-1}.

Electrochemical measurements

Working electrodes were fabricated by mixing the final product powders, acetylene black (as a conductive agent), and polyvinylidene fluoride (as a binder) in N-methyl-2-pyrrolidone at a weight ratio of 80:10:10. The slurry was uniformly plastered on a copper foil current collector via doctor blade processing, followed by vacuum drying at 120 °C for 12 h. A two-electrode 2016 type coin cell was used to assess the electrochemical performance. A lithium metal electrode was used as a counter electrode. The organic electrolyte was 1.0 M $LiPF_6$ dissolved in a mixture of ethylene carbonate (EC) and dimethyl carbonate (DMC) (1:1, v/v) plus 5 v% vinylene carbonate. The separator was a polypropylene separator (Celgard2400). Electrochemical test cells were assembled in an argon-filled glove box (Etelux, Lab2000) in which H_2O and O_2 concentration were kept below 1 ppm. The galvanostatic charge–discharge measurements were carried out (Neware, BTS-3000) in the voltage range of 3.0 to 0.01 V (vs. Li/Li+) at room temperature (25±1 °C). The cyclic voltammograms (CV) and electrochemical impedance spectroscopy (EIS) were measured on an electrochemical workstation (CHI660D) at a scanning rate of 0.5 mV·s^{-1}. EIS were recorded by applying an AC voltage of +/-10 mV over the frequency range from 10^5 to 0.01 Hz.

Results and discussion

Structure and morphology

The 3D Si@CNT/GS nanostructured composite was constructed by the template-free methodology that can be scaled-up easily. It is anticipated that the aromatic regions of graphene oxide (GO) can interact with the side walls of the CNTs through $\pi-\pi$ stacking interactions [**28**], which facilitates good dispersion of CNTs in the GO matrix during synthesis. We improve the binding strength between the Si NPs and an electrically conducting network by ultrasonic treatment. The existence of inactive SiOx on the surface of Si nanoparticles is beneficial to enhance the interfacial adhesion between silicon, CNT and graphene. The overall mixture self-assemble to form a robust nanoheterostructure. The low-magnification SEM images (**Fig. 2a**) show that the Si@CNT/GS nanocomposites are micrometer-sized nanocomposite with rough and wrinkled surface. **Fig. 2b** shows that the CNTs are uniformly interweaved inside the thermally reduced graphene oxide sheets, forming a 3D CNT/GS matrix which effectively confines well dispersed Si NPs. **Fig. 2c** reveals the good connection among Si NPs, CNTs, and GS.

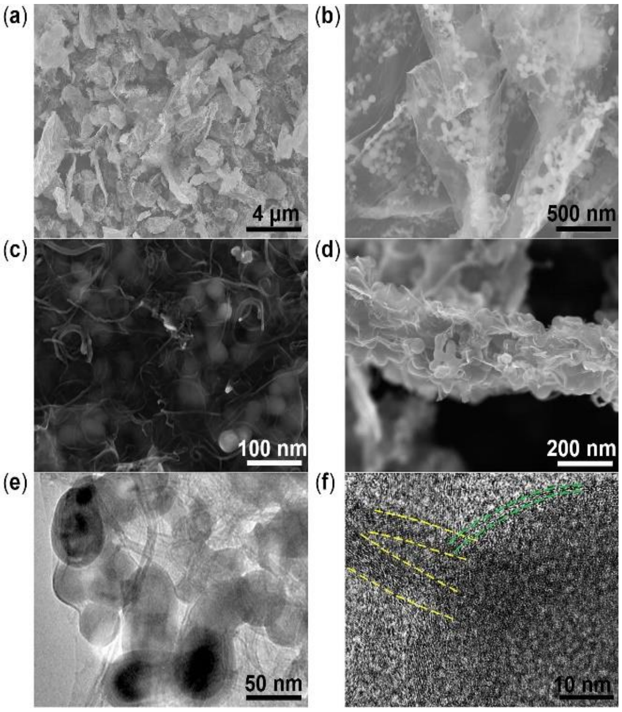

Fig. 2. (a, b) Low- and (c, d) high magnification SEM images of the Si@CNT/GS nanocomposites; (e) Low- and (f) high magnification TEM images of the Si@CNT/GS nanocomposites.

Almost all Si NPs are linked by more than one CNT. The cross section SEM image (**Fig. 2d**) indicates that CNTs provide good transport path through the entire 3D Si@CNT/GS nanocomposites. Jinbao Zhao et al. reported a novel polyvinyl alcohol (PVA) hydrogel method in which the CNTs form a porous network acting both as conductive agent for electron transfer and buffer space to accommodate huge Si volume change during lithiation/delithiation process [**39**]. The TEM image of Si@CNT/GS (**Fig. 2e**) further reveals that net-link among the confined Si NPs (20-50 nm in diameter), CNTs, and GS. The Si nanoparticles showed obvious core-shell structure, which was a uniform layer of amorphous SiOx. It has been reported that the existence of inactive SiOx on the surface of Si nanoparticles is benifical to enhance the interfacial adhesion between silicon, CNT and graphene, which can maintain the structural integrity of electrodes during charge/discharge process. Furthermore, SiOx can react with Li to produce effective Li_2O buffer to keep the excellent cycle retention [**29**]. The HR-TEM images in **Fig. 2f** demonstrates a typical Si NP that is partially wrapped by GS (≤3 layers) (green lines) while linked to several CNTs (yellow lines). Such a unique geometric series connection of electrochemically active materials within a CNT/GS matrix can effectively suppress the aggregation and the damaging effect of volume change of nanoparticles, and enhance electrode stability against cycling processes for lithium storage.

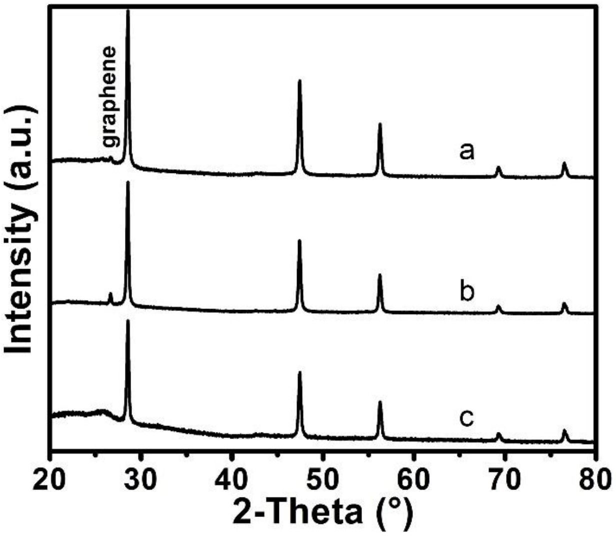

Fig. 3. XRD patterns of (a) Si@CNT/GS, (b) Si@GS, and (c) Si@CNT

The obtained Si@CNT/GS nanocomposites were characterized by X-ray diffraction (XRD). As shown in **Fig. 3a**, the peaks at 28.6°, 47.5°, 56.3°, 68.5°, and 75.7° can be assigned to the (111), (220), (311), (400), and (331) reflections of Si (JCPDS No. 27-1402), respectively. A diffraction hump appearing in the range of 24-28° is attributed to the stacking of graphene sheets [**28**]. For comparison, the XRD patterns of Si@GS (**Fig. 3b**) and Si@CNT (**Fig. 3c**) are also provided, and all the main peaks can be assigned to the standard profiles of silicon.

X-ray photoelectron spectroscopy (XPS) measurements of the Si@CNT/GS naocomposites were performed in the range of 0 to 1200 eV together with Si@CNT/GO for comparison. As shown in **Fig. 4a** and **4b**, the XPS spectra of Si@CNT/GO clearly indicated a considerable degree of oxidation with four different peaks at 284.5, 286.6, 287.8, and 289.0 eV, corresponding to C=C/C-C in aromatic rings, C–O (epoxy and alkoxy), C=O, and COOH groups, respectively [**30**]. The intensity of Si was very weak because the Si NPs are embedded in the CNT/GS matrix and had limited areal coverage. The Si@CNT/GS nanocomposites spectrum indicated the presence of carbon, oxygen, and silicon, arising from Si NPs, CNTs, and GS (**Fig. 4c** and **4d**) [**31**]. Compared with Si@CNT/GO, the intensities of O peak and peaks due to carbon bonded to oxygen decreased substantially in Si@CNT/GS, indicating that most of the oxygen-containing functional groups were removed after thermal reduction.

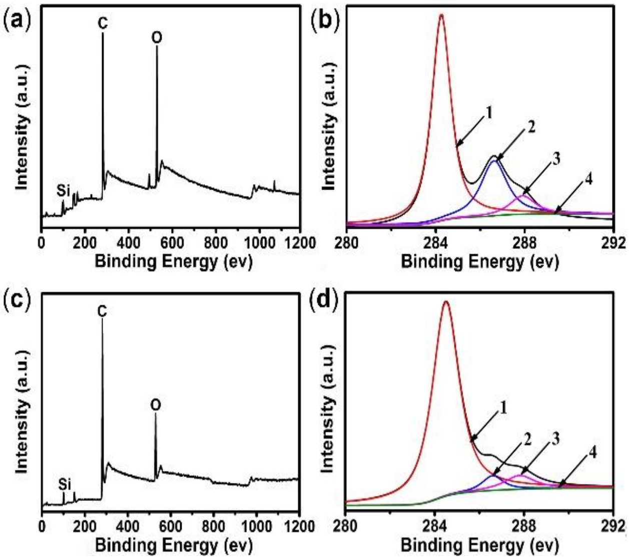

Fig. 4. XPS spectra of (a) Si@CNT/GO, survey scan; (b) C1s of Si@CNT/GO; (c) Si@CNT/GS, survey scan; and (d) C1s of Si@CNT/GS. The peaks marked with 1, 2, 3, and 4 correspond to C=C/C-C in aromatic rings, C–O (epoxy and alkoxy), C=O, and COOH groups, respectively.

Fig. S1 shows the Raman spectra of Si@CNT/GS nanocomposites and Si@CNT/GO, the spectrum of these samples was composed of the D band at around 1350 cm^{-1}, the G band at 1595 cm^{-1}, and three peaks around 263, 516, and 950 cm^{-1}. The G-band is characteristic of graphitic sheets, corresponding to a well-defined sp^2 carbon-type structure; whereas the D-band can be attributed to the presence of defects within the hexagonal graphitic structure [**32**]. The presence of such defects may help the efficient access for Li ions to diffuse in and out of the Si NPs [**33**]. The other three scattering around 263, 516, and 950 cm^{-1} corresponded to pure Si NPs. Thus, a smaller I_D/I_G ratio indicates lower defects and disorders of the graphitized structures [**34**]. The I_D/I_G ratio increased from 1.09 for Si@CNT/GO to 1.22 for the Si@CNT/GS nanocomposites, which indicated a decrease in the average size and an increase in the number of sp^2 graphite domains. A similar increase in the I_D/I_G ratio after reduction has been observed in other systems [**30**].

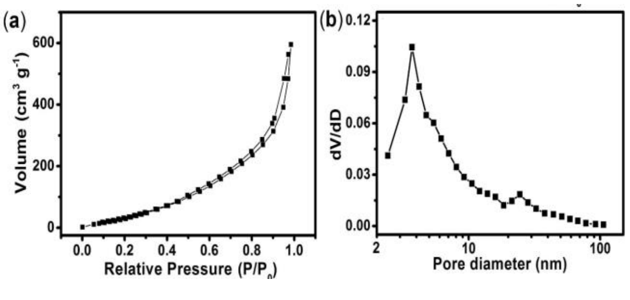

Fig. 5. (a) Nitrogen adsorption and desorption isotherm and (b) pore-size distribution of Si@CNT/GS nanocomposites.

The 3D porous structure of the Si@CNT/GS nanocomposites was probed by nitrogen isothermal adsorption/desorption measurement (**Fig. 5**). The Brunauer–Emmett–Teller specific surface area of the Si@CNT/GS nanocomposite, calculated from the isotherm in **Fig. 5a**, was 98 m^2·g^{-1}. Base on the Barrett–Joyner–Halenda model, the pores ranged mostly between 3 and 100 nm, with a distribution showing two peaks at 4 and 25 nm (**Fig. 5b**). The high surface area of the Si@CNT/GS nanocomposites in association with its meso- and macroporous features offered efficient ionic transport pathways, thus enhancing the electrochemical performance.

The thermal properties and compositions of the Si@CNT/GS nanocomposites were determined by TGA in air at a heating rate of 10 °C·min^{-1}. As shown in **Fig. S2**, the Si nanoparticles were stable against oxidation up to 500 °C, and the mass increased by only 5.5% at 800 °C due to the slight oxidation of Si. An abrupt weight loss occurs during 300-400 °C for CNT and 500-600 °C for graphene, indicating decomposition and oxidation in air. As a composite of the above three components, the Si@CNT/GS mainly lost weight between 500 °C and 650 °C owing to the combustion of graphene and CNT in air. The results showed that the weight fraction of silicon in the Si@CNT/GS to be 71 wt%.

Electrochemical performance

The cyclic voltammetry (CV) curves of the Si@CNT/GS nanocomposites (**Fig. 6a**) exhibits similar electrochemical characteristics as that of pristine Si powders [**35**]. The broad cathodic peak at around 0.72 V appeared in the first cycle, but not in subsequent cycles, which could be attributed to the formation of solid electrolyte interphase (SEI) on the electrode surface [**36**]. The small peak at 1.3 V could be related to the reactions of the remaining oxygen functionalities in graphene sheets [**31**]. The large cathodic current between 0 and 0.2 V was due to the formation of Li–Si alloy phases, while the two peaks at 0.31 and 0.55 V at the anodic sweep could be ascribed to dealloying of the Li–Si alloys [**37**]. The electrochemical performance of Si@CNT/GS was evaluated by galvanostatic discharge-charge measurements at a current density of 500 mA·g^{-1} (**Fig. 6b**). The initial capacity of Si@CNT/GS was 1885 mAh·g^{-1}, significantly higher than that of Si@GS and Si@CNT (1739 mAh·g^{-1} and 1498 mAh·g^{-1}, respectively.) The capacity of all three electrodes fell in the first 10 to 30 cycles, probably due to the formation of a solid electrolyte interface (SEI) on the Si NPs and the reaction of oxygen-containing functional groups on the graphene with lithium ions [**38**]. The cycling performance of Si@CNT/GS was superior to that of Si@GS and Si@CNT (**Fig. 6c**-a, d, and e). Starting from the tenth cycle, the reversible capacity of Si@CNT/GS began to stabilize, eventually reaching1362 mAh·g^{-1} at 500 mA·g^{-1} after 500 cycles (**Fig. 6c**). In contrast, both the Si@CNT and Si@GS exhibited an inferior cycling performance, the capacity of Si@GS gradually decreased from 1739 to 749 mAh·g^{-1} after 100 cycles, while the capacity of Si@CNT rapidly decayed from 1498 to 493 mAh·g^{-1} after 100 cycles.

The effect of CNT loading on the electrochemical property of the Si@CNT/GS nanocomposites was also investigated using three samples of Si:GO:CNT ratios 60:30:30, 60:30:15, and 60:30:5. For all three samples, stable reversible capacity was obtained after 100 cycles as shown in **Fig. 6**c-a-c. The samples with higher CNT contents showed better cycling performance and higher reversible capacities. The data demonstrated the clear benefit of the CNTs, most likely due to their ability to entangle the Si nanoparticles to improve dispersion of these nanoparticles and to preserve good electrical contact.

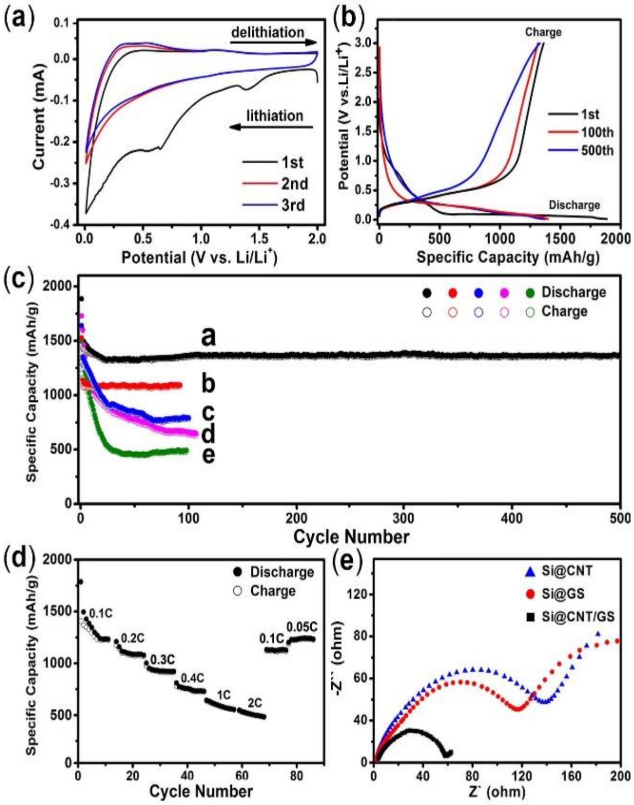

Fig. 6. (a) Cyclic voltammetry profiles of the Si@CNT/GS nanocomposites; (b) Galvanostatic discharge-charge profiles of Si@CNT/GS at a current density of 500 mA·g^{-1}; (c) Cycling performance of Si@CNT/GS with the ratio of Si:GO:CNT= 60:30:15 (a), 60:30:30 (b), 60:30:5 (c), Si@GS with the ratio of Si:GO= 60:45(d), and Si@CNT the ratio of Si:CNT= 60:45 (e) at a current density of 500 mA·g^{-1}; (d) Cycling performance of Si@CNT/GS at various current densities; (e) Nyquist plots of Si@CNT/GS, Si@GS, and Si@CNT electrodes.

The rate capacity of the Si@CNT/GS nanocomposites with a Si:GO:CNT ratio of 60:30:15 was investigated (**Fig. 6d**). A high rate capability was found. For example, at a current density of 8400 mA·g^{-1} (equal to a current rate of 2 C), Si@CNT/GS still delivered a favorable capacity of 504.8 mAh·g^{-1}. When the current rate was returned to 500 mAh·g^{-1}, the stable high capacity of Si@CNT/GS (1133 mAh·g^{-1}, 91.8% of the initial reversible capacity) was recovered. To verify the superior electrochemical performance of Si@CNT/GS, Si@GS, and Si@CNT electrodes, AC impedance measurements were performed after the rate capability test. The Nyquist plots (**Fig. 6e**) show that the diameter of the semicircle for Si@CNT/GS in the high–medium frequency region was much smaller than those of Si@GS and Si@CNT, indicating lower contact and charge-transfer impedances of Si@CNT/GS compared with Si@GS and Si@CNT [**36**].

The above results clearly demonstrate the enhanced cycling and rate performance of Si@CNT/GS as an anode material for lithium storage, which can be attributed to the rationally designed 3D architecture. First, the conductive CNTs effectively enhance the physical and electrical contact of each Si NPs with the surrounding 3D conductive matrix, thereby maximizing the effective electrochemical utilization of the active materials and ensuring a reversible lithium insertion/extraction process even at high current rates. Second, the excellent elasticity of 3D CNT/GS hierarchically nanostructured matrix provides a framework that can easily accommodate the volume changes of Si NPs during electrochemical processes. Third, this 3D CNT/GS nanostructured matrix is filled with conductivity paths in both the planar direction of graphene sheets and also the axial direction by the CNTs, forming a 3D conductive network. Moreover, this 3D CNT/GS nanostructured matrix has meso-/macro-pores and a high surface area. Together, these properties facilitate easy electron conduction and ion mobility through the electrode, which allow fast electron and ion transport and result in the much improved reversible capacity and rate capability.

Conclusion

3D Si@CNT/GS nanocomposites comprising porous CNT/GS nanostructured matrix and embedded dispersed Si NPs were fabricated. Si NPs, CNTs, and rGO play important roles in this nanostructured matrix, it is well known that Si NPs provide high capacity, and rGO ensures high conductivity of the overall structure and provides sufficient void space to buffer the volume changes of the Si NPs during lithiation/delithiation and the CNT acts as support in conjunction with Si NPs and provides additional conductive channels. This unique architecture provides protection against the aggregation and volume changes of silicon active materials, and ensures favorable transport kinetics for both electrons and lithium ions. Superior cycling performance (1362 mAh g^{-1} at 500 mA·g^{-1} over 500 cycles) and excellent rate capability (504.8 mAh·g^{-1} at 8400 mA·g^{-1}) were achieved when the Si@CNT/GS nanocomposites was used as anode material for lithium storage.

Acknowledgements

This research was supported by the National Natural Science Foundation of China (No. 51425202), Natural Science Foundation of Jiangsu Province (BK20160093),and the Project Funded by the Top-notch Academic Programs Project of Jiangsu Higher Education Institutions (TAPP).HHK is supported by the US DOE through the Center for Electrical Energy Storage (DE-AC-02-06CH11357).

Author's contributions

Conceived the plan: Dafang He, Fengjuan Bai, Ningzhong Bao; Performed the expeirments: Lixian Li, Fengjuan Bai; Data analysis: Dafang He, Lixian Li, Chenyang Zha, Liming Shen; Wrote the paper: Dafang He, Lixian Li, Liming Shen, Harold H. Kung. Authors have no competing financial interests.

References

1. Tarascon, J.M.; Armand, M.; *Nature*, **2001**,*414*,359.
   DOI: 10.1038/35104644
2. Armand, M.; Tarascon, J. M.; *Nature*, **2008**,*451*,652.
   DOI: 10.1038/451652a
3. Goodenough, J. B.; Kim, Y.; *Chem.Mater.*,**2010**,*22*,587.
   DOI: 10.1021/cm901452z

4. Zha, C. Y.; He, D. F.; Zou, J. W.; Shen, L. M.; Zhang, X. Y.; Wang, Y. F.; Kung, H. H.; Bao, N. Z.; *J. Mater. Chem. A*, **2014**,*2*,16931.
DOI: 10.1039/c0cs00136h
5. Boukamp, B. A.; Lesh, G. C.; Huggins, R. A.; *J. Electrochem. Soc*.,**1981**,*128*, 725.
DOI: 10.1002/chin.198131022
6. Kasavajjula, U.; Wang, C. S.; Appleby, A. J.; *J. Power Sources*,**2007**,*163*,1003.
DOI: 10.1016/j
7. Magasinski, A.; Dixon, P.; Hertzberg, B.; Kvit, A.; Ayala, J.; Yushin, G.; *Nat. Mater.*,**2010**,*9*,353.
DOI: 10.1038/nmat2749
8. Poizot, P.; Laruelle, S.; Grugeon, S.; Dupont, L.; Tarascon, J. M.; *Nature*,**2000**, *407*,496.
DOI: 10.1038/407496a
9. Hu, Y.S.; Titirici, R. M. M.; Mueller, J. O.; Schloegl, R.; Antonietti, M.; Maier, J.; *Angew. Chem. Int. Ed*. **2008**,*47*,1645.
DOI: 10.1002/anie.200704287
10. Cao, F. F.; Deng, J.W.; Xin, S.; Ji, H. X.; Schmidt, O. G.; Wan, L. J.; Guo, Y. G.; *Adv. Mater.*,**2011**,*23*,4415.
DOI: 10.1002/adma.201102062.
11. Chan, C. K.; Peng, H.; Liu, G.; McIlwrath, K.; Zhang, X. F.; Huggins, R. A.; Cui, Y.; *Nat. Nanotechnol.*,**2008**, *3*,31.
DOI: 10.1038/nnano.2007.411
12. Song, T.; Xia, J. L.; Lee, J. H.; Lee, D. H.; Kwon, M. S.; Choi, J. M.; Wu, J.; Doo, S. K.; Chang, H.; Park, W.; *Nano Lett.*,**2010**,*10*, 1710.
DOI: 10.1021/nl100086e
13. Hertzberg, B.; Alexeev, A.; Yushin, G.; *J. Am. Chem. Soc.*,**2010**,*132*, 8548.
DOI: 10.1021/ja1031997
14. Park, M. H.; Kim, M. G.; Joo, J.; Kim, K.; Kim, J.; Ahn, S.; Cui, Y.; Cho, J.; *Nano Lett.*,**2009**,*9*,3844.
DOI: 10.1021/nl902058c
15. Jia, H.; Gao,P.; Yang, J.; Wang, J.; Nuli, Y.; Yang, Z.; *Adv. Energy Mater*.,**2011**,*1*,1036.
DOI: 10.1002/aenm.201100485
16. Yu, Y.; Gu, L.; Zhu, C. B.; Tsukimoto, S.; van Aken, P. A.; Maier, J.; *Adv. Mater*.,**2010**,*22*,2247.
DOI: 10.1002/adma.200903755
17. Ng, S. H.; Wang, J. Z.; Wexler, D.; Konstantinov, K.; Guo, Z. P.; Liu, H. K.; *Angew. Chem. Int. Ed.*,**2006**,*45*,6896.
DOI: 10.1002/ange.200601676
18. Magasinski,A.; Dixon, P.; Hertzberg, B.; Kvit, A.; Ayala, J.; Yushin, G.; *Nat. Mater.* ,**2010**,*9*,353.
DOI: 10.1038/nmat2749
19. Novoselov, K. S.; Geim, A. K.; Morozov, S. V.; Jiang, D.; Zhang, Y.; Dubonos, S. V.; Crigorieva, I. V.; Firsov, A. A.; *Science*, **2004**, *306*,666. **DOI:** 10.1126/science.1102896
20. Geim, A. K.; Novoselov, K. S.; *Nat. Mater.*,**2007**,*6*,183.
DOI: 10.1038/nmat1849
21. Tiwari, A.; Dhakate, S. R.; *International Journal of Biological Macromolecules*, **2009**, 44, 408.
DOI: 10.1016/j.ijbiomac.2009.03.002
22. Chang, J. B.; Huang, X. K.; Zhou, G. H.; Cui, S. M.; Hallac, P. B.; Jiang, J. W.; Hurley, P. T.; Chen, J. H.; *Adv. Mater.*,**2014**,*26*,758.
DOI: 10.1002/adma.201302757
23. Wang, W.; Kumta, P. N.; *ACS Nano*,**2010**,*4*,2233.
DOI: 10.1021/nn901632g
24. Cui, L. F.; Hu, L. B.; Choi, J. W.; Cui, Y.; *ACS Nano*,**2010**,*4*,3671.
DOI: 10.1021/nn901632g
25. Lee, J. K.; Smith, K. B.; *Chem. Commun.*,**2010**,*46*,2025.
DOI: 10.1039/b919738a
26. Zhao, X.; Hayner, C. M .; Kung, M. C.; Kung, H. H.; *Adv. Energy Mater.*,**2011**,*1*,1079.
DOI: 10.1002/aenm.201100426
27. He, D. F.; Bai, F. J.; Li, L. X.; Shen, L. M.; Kung, H. H.; Bao, N. Z.; *Electrochimi. Acta*,**2015**,*169*,409.
DOI: 10.1016/j.electacta.2015.04.090
28. He, D. F.; Shen, L. M.; Zhang, X. Y.; Wang, Y. F.; Bao, N. Z.; Kung, H. H.; *AIChE J.*,**2015**,*60*,2757.
DOI: 10.1002/aic.14499
29. Bai, Z. J.; Yu, Y. Y.; Kung, H. H.; Wang, B.; Jiang, J. M.; *J. Powder Sources*,**2016**,*306*,42. **DOI:** 10.1016/j
30. Wu,J. X.; Qin, X. Y.; Zhang, H. R.; He, Y. –B.; Li, B. H.; Ke, L.; *Carbon* ,**2015**,*84*,434.
DOI: 10.1016/j.carbon.2014.12.036
31. Park, S. H.; Kim, H. H.; Ahn, D. J.; Lee, S. I.; Roh, K. C.; Kim, K. B.; *Electrochem. Commun.*,**2013**,*34*,117.
DOI: 10.1016/j.elecom.2013.05.028
32. Su, M. R.; Wang, Z. X.; Guo, H. J.; Li, X. H.; Huang, S. L.; Xiao, W.; Gan, L.; *Electrochimica Acta*,**2014**,*116*,230.
DOI: 10.1016/j.electacta.2013.10.195
33. Kim,H.; Son, Y.; Park, C.; Cho, J.; Choi, H. C.; *Angew. Chem. Int. Ed*.,**2013**,*52*,5997.
DOI: 10.1002/anie.201300896
34. Yang, S. N.; Li, G. R.; Zhu, Q.; Pan, Q. M.; *J. Mater. Chem.*, **2012**,*22*,3420. **DOI:** 10.1039/c2jm15232k
35. Yun, Q. B. ; Qin, X. Y.; Lv, W.; He, Y. B.; Li, B. H.; Kang, F. Y.; *Carbon* ,**2015**,*93*,59.
DOI: 10.1016/j.carbon.2015.05.032
36. Chou, S.L.; Wang, J. Z.; Choucair, M.; Liu, H. K.; Stride, J. A.; Dou, S. X.; *Electrochem. Commun.*,**2010**,*12*,303.
DOI: 10.1016/j.elecom.2009.12.024
37. Zhu,Y. H.; Liu, W.; Zhang, X. Y.; He, J. C.; Chen, J. T.; Wang, Y. P.; Cao, T. B.; *Langmuir*,**2013**,*29*,744.
DOI: 10.1021/la304371d
38. Zhou, M. T.; Cai, W.; Pu, F.; Chen, H.; Wang, Z.; Zhang, H. Y.; Guan, S. Y.; *ACS Appl. Mater. Inter*.,**2013**,*5*,3449.
DOI: 10.1021/am400521n
39. Chen, D. Q. ;Liao, W. J. ; Yang, Y.; Zhao, J. B. ; *Journal of Power Sources*,**2016**, *315* , 236.
DOI: 10.1016/j.jpowsour.2016.03.051
40. Wang, W.; Kumta, P. N.; *Acs Nano*, **2010**, *4*,2233.
DOI: 10.1021/nn901632g
41. Wang, X.H.; Susantyoko, R. A.; Sun, L.M.; Fan,Y.; Zhang,Q.; *Nano Energy* , **2014**, *8*,71.
DOI: 10.1016/j.nanoen.2014.05.020
42. Epur, R.; Ramanathan, M.; Datta, M. K.; Hong, D. H.; Jampani, P. H.; Gattu, B.; *Nanoscale*, **2015**,*7*, 3504.
DOI: 10.1039/c4nr04288c
43. Ye, Y. ; Xie, X. ; Rick, J. ; Chang , F.; Hwang, B. ;*J. Power Sources*, **2014**,*247*,991.
DOI: 10.1016/j.jpowsour.2013.08.048
44. He, D.F.; Bai, F.J.; Li, L.X.; Shen, L.M.; Kung, H. H.; Bao, N.Z.; *Electrochimica Acta*, **2015**,*169*, 409.
DOI: 10.1016/j.electacta.2015.04.090
45. Tao, H. C.; Yang, X. L.; Zhang, L. L.;Ni, S. B.; *Ionics*,**2014**, *21*, 617.
DOI: 10.1007/s11581-014-1218-9
46. Liu, H.; Shen, Z.G.; Liang, S.S.; Liu, L.; Yi, M.; Zhang, X.J.;Ma, S.L.;*New Journal of Chemistry*,**2016**,*40*,7053.
DOI: 10.1039/c6nj01234e
47. Luo Z.W.;Ding,T.T.;Dai,J.N.;Chen,C.Q.;*International Journal of Electrochemical Science*, **2016**,*11*,4794.
DOI: 10.20964/2016.06.4

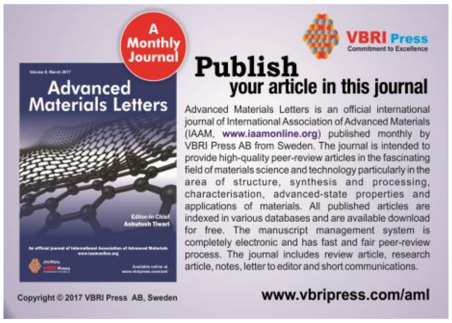

Supporting Information

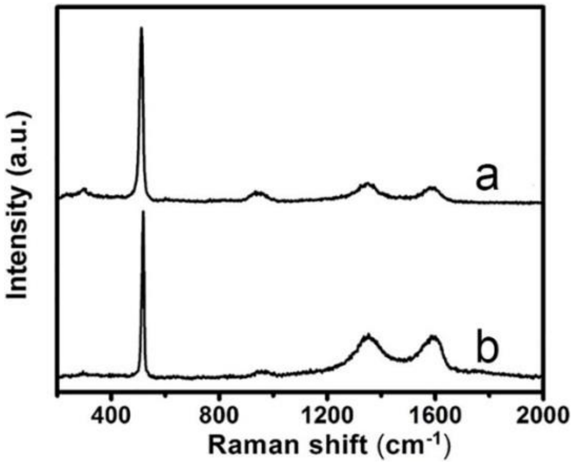

Fig. S1. Raman spectra of (a) Si@CNT/GS, (b) Si@ CNT/GO.

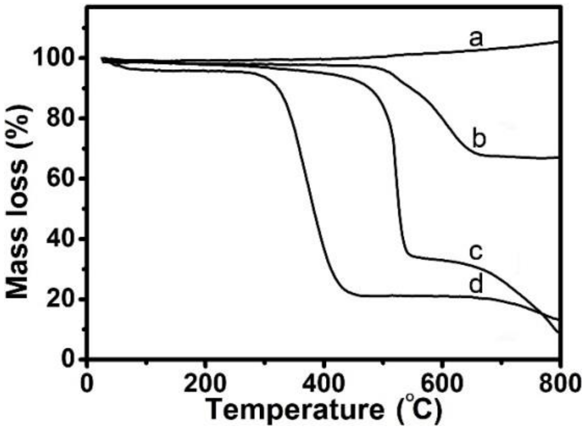

Fig. S2. TGA curves of (a) Si NPs, (b) Si@CNT/GS, (c) GS, and (d) CNT.

Table S1. Capacity comparison of some Si-based lithium ion battery anodes

Typical examples	Electrochemical properties	Ref.
Nanostructured Hybrid Silicon/Carbon Nanotube Heterostructures	The Si/CNTs hybrid anode demonstrate a capacity 1000 mAh/g even after 100 cycles at C/10 rate	40
Consisting a pore size graded thick CNT–Si film	more than 3000 mAh/cm3 after 200 cycles at 840mA/g	41
Scribable multi-walled carbon nanotube-silicon nanocomposites	At the end of 50 cycles, capacities close to 2000 mAh/g were obtained when cycled at the current of 300 mA/g	42
on-covalently bonded graphene and silicon nanoparticles	A capacity of 803 mAh/g in 100 cycles at the current of 200 mA/g.	43
Sandwich-structured Si nanoparticles–graphene nanocomposite	A reversible capacity of 746 mAh/g after 160 cycles at 1000 mA/g	44
Reduced graphene oxide/porous Si composite	a reversible capacity of about 815 mAh/g at 100 mA/g after 50 cycles.	45
Liquid-exfoliated pristine graphene/Si composite	a high reversible capacity of 700 mAh/g after 100 cycles at 100 mA/g	46
Reduced Graphene Oxide Encapsulated N-type Si Nanoparticles	specific capacity remaining at 1529 mAh/g for over 200 cycles at 0.2C rate	47
Three-dimensional Nanocomposites of Graphene/Carbon Nanotube Matrix-Embedded Si Nanoparticles	a high reversible capacity of 1362 mAh·g-1 at 500 mA·g-1 over 500 cycles	